

AERODYNAMIC ANALYSIS OF CAMBER MORPHING AIRFOILS USING PARTICLE IMAGE VELOCIMETRY AND COMPUTATIONAL FLUID DYNAMICS METHODS

Marta Marciniuk¹, Łukasz Kiszkowiak², Paweł Piskur³, Łukasz Malicki¹, Katarzyna Strzelecka¹, Krzysztof Sibilski² & Stanisław Kachel²

¹Wrocław University of Science and Technology, Faculty of Mechanical and Power Engineering, Department of Cryogenics and Aerospace Engineering, 27 Wybrzeże Stanisława Wyspiańskiego Str., 50-370, Wrocław, Poland, marta.marciniuk@pwr.edu.pl, lukasz.malicki@pwr.edu.pl, katarzyna.strzelecka@pwr.edu.pl, tel. +48662122172, +48604860062

²Military University of Technology, Faculty of Mechatronics, Armament and Aerospace, gen. Sylwestra Kaliskiego 2, 00-908, Warsaw, Poland, lukasz.kiszkowiak@wat.edu.pl, krzysztof.sibilski@wat.edu.pl, stanislaw.kachel@wat.edu.pl, tel. +48261837374

³Polish Naval Academy of the Heroes of Westerplatte, Faculty of Mechanical and Electrical Engineering, Śmidowicza Street 69, 81-127 Gdynia, Poland, p.piskur@amw.gdynia.pl, tel. +48502509638

Abstract

Morphing airfoils are a wide range researched branch of aviation these days. They could efficiently reduce drag and provide better aerodynamic performance due to a smooth transition between the leading and trailing edges when slightly deflected. One interesting approach to modifying aerodynamic performance is drag production. The creation of drag is especially useful when it comes to the landing phase of an aircraft, as it allows the reduction of the approach speed and landing distance. Micro UAVs are burdened with the risk of damage during landing. Existing solutions for micro UAV landing show a number of disadvantages. This paper presents an innovative approach to camber morphing airfoils utilizing not only their abilities to improve aerodynamic performance but also to create drag when extended significantly. The authors performed experiments in a hydrodynamic tunnel using Particle Image Velocimetry (PIV) and then compared the results with Computational Fluid Dynamics (CFD) simulation solutions. The results show a nearly linear increase of drag coefficient with the increase of setting angle and a non-linear increase of lift force coefficient for setting angles from -6° to 6° .

Keywords: morphing airfoil, Unmanned Aircraft Vehicle, Particle Image Velocimetry, Computational Fluid Dynamics.

1. Introduction

Camber morphing airfoils are widely studied adaptive wing structures designed to change shape and adapt to a wide variety of flight conditions. The development of materials in the last few decades enabled researchers to conduct various technical solutions for morphing wings[1], allowing them to create more revolutionary concepts [2]. These modern structures exhibit a significant increase in the aerodynamic efficiency of aircraft wings [3]. Majid and Jo [4] conducted a numerical aerodynamic performance study at a low Reynolds number. In their research, they concluded that morphing airfoils are a promising solution for aerodynamically efficient aircraft. Numerical simulations showed an 18,7% increase in lift-to-drag ratio for morphing airfoils compared to airfoils with traditional mechanisation.

One particular area of interest within aviation society is micro Unmanned Aerial Vehicles (UAVs). Micro UAVs are the most developed branch of aviation these days [5]. They enable the execution of dangerous human missions in hazardous or inaccessible locations [6]. The assets of micro UAVs are valued by private, commercial and military industries. Private and commercial use include photography, photogrammetry, commercial monitoring, crops monitoring, environmental studies, fire

surveillance, linear and point infrastructure monitoring and highway traffic control [7, 8, 9]. Military applications include surveillance, search and rescue operations, communication, battlefield survival, identifying targets, detection of weapons of mass destruction and meteorological information collection [10, 11].

Implementing morphing airfoils to micro UAVs appears to be a valuable asset, as morphing airfoils could provide better aerodynamic performance due to a smooth transition between the leading and trailing edges [12]. Nevertheless, the concept of morphing airfoils extends beyond improving aerodynamic efficiency. Morphing airfoils are a promising solution, especially in landing manoeuvres, which are risky due to aircraft damage. Micro UAVs commonly have removed landing gears to reduce the mass and drag coefficient of the structure. To further reduce the mass and complexity of the structure, they usually are not equipped with flaps. In consequence, fixed-wing micro UAVs need long and smooth landing distances as their approach speed is high [13]. To overcome this inconvenience, constructors developed a few alternative landing methods, but all of them have many disadvantages. Scan Eagle UAV is utilised for landing two 15-meter high poles with extended rope, which intercepts the aircraft [10]. This method is expensive and requires specialized equipment for transportation and placing pillars. This comes with many difficulties when considering changes in the landing spot of an aircraft. It also demands a trained group of people to capture the micro UAV. Jouvet et al. [14] for their glacier monitoring micro UAV used the net landing method. The aircraft approaches a point designated behind the net and is captured by the net. The authors pointed out that the wing gusts caused significant difficulties in maintaining the desired trajectory, which forced the UAV operator to override the autopilot to safely land the aircraft. Wind gusts are not the only disadvantage of this solution. As mentioned in the previous method, net landing produces several logistic problems, including changing landing spots, transportation, and crew training.

Nevertheless, the most common landing method for micro UAVs remains belly landing, which entails problems such as a high landing distance, high approach speed, and smooth and flat terrain. This causes severe damage to micro UAV during landing, as mentioned in Michalska's et al. research [15]. Authors present that 72% of UAVs are damaged during aerial operational time, with specific emphasis on the landing phase. The most common damaged components are winglets and fuselage. Wings were not taken into consideration in this study.

Morphing airfoils can improve aircraft aerodynamic performance by reducing drag and, when deflected significantly, creating drag. The high amount of drag can lower the approach speed and significantly decrease the landing distance, which will undoubtedly lower the damage during micro UAV landing. When slightly deflected, morphing airfoils can reduce the influence of wind gusts on micro UAVs and enhance autopilot capabilities.

The authors of this work examined airfoils in different morphing phases, from non-morphed to fully morphed. The target aircraft was a micro Unmanned Aerial Vehicle (micro UAV). The purpose of this work was to present the research methods authors utilized and the abilities of morphing airfoil to increase lift force and to show it is capable of creating drag. For this purpose, one of the created airfoils was chosen, and the results are presented based on this representative example. The research was conducted both numerically and experimentally. Both investigations were obtained in a two-dimensional environment. Experiments were performed in the hydrodynamic tunnel using the Particle Image Velocimetry (PIV) method. Camber morphing airfoil models were prepared using the additive manufacturing method. Numerical simulations were based on $k-\omega$ SST turbulence model in OpenFOAM environment.

2. Materials and methods

2.1 Morphing airfoils

The authors prepared six airfoils based on the NACA24012 profile. The 25% of MAC from the leading edge of the NACA24012 airfoil was fixed, and only the back section of the airfoil was varied. All six geometries are presented in Figure 1. The red square highlights the chosen geometry for a representative example.

The *Airfoil 3* geometry is presented in the Figure 2. The airfoil chord length is c=0.246m, and the airfoils' angle of attack value is $\alpha=13^{\circ}$. As the camber morphing airfoils have the trailing edge moved downwards, the base angle of attack has a non-zero value, and authors use the expression *setting* angle when it comes to changes of the airfoil angle to flow direction.

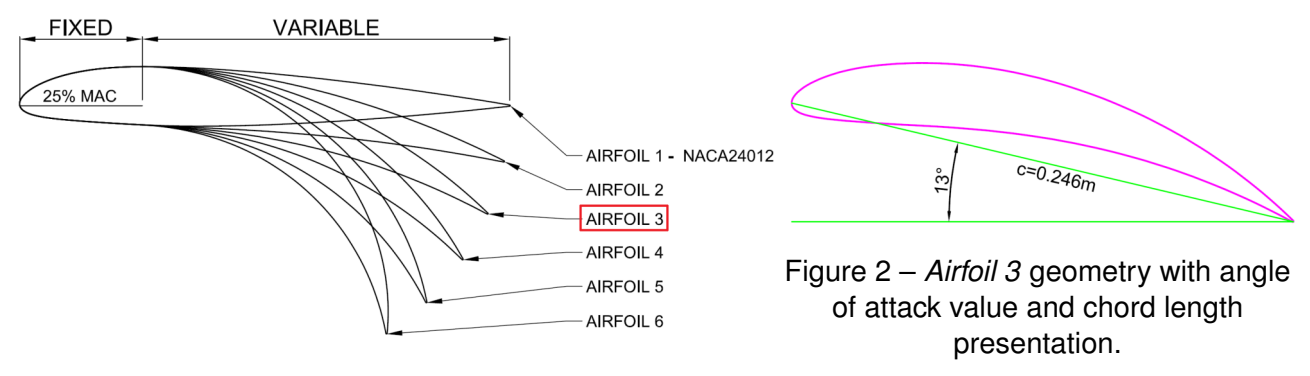


Figure 1 – Created geometries of camber morphing airfoil.

From the two-dimensional (2D) geometry, a three-dimensional (3D) wing model was created. The model was then produced using the additive manufacturing method. Further preparation of the created model required filling, grinding and painting to obtain a smooth model surface for hydrodynamic tunnel experiments (Fig 3).

2.2 Hydrodynamic water tunnel

The observation of the wake structures behind the airfoil and turbulence distribution is crucial for understanding the processes occurring in the boundary layer of an airfoil. Water tunnels are perfect for flow observations as water has about 800 times higher density compared to air. Visualising the flow is also much easier in water than in the air due to water's higher dynamic viscosity.

Experiments were performed in the hydrodynamic water tunnel (Fig. 4), placed in the Military University of Technology in Warsaw, with closed fluid circulation.



Figure 3 – Presentation of airfoils prepared for Figure 4 – The Rolling Hills Research Corporation experiments. hydrodynamic water tunnel.

The measuring chamber has a rectangular test section with the dimensions of $610mm \times 915mm$. The tunnel is equipped with a bracket that ensures the movement of a test model in three dimensions: a

water flow velocity meter and a thermometer in the test chamber. The measurement of both values is used to calculate the Reynolds number for given conditions in the course of the experiment. The range of water flow velocities in the hydrodynamic tunnel varies from 0 to 280mm/s [16, 17, 18, 19]. The experiment was performed in the temperature of $26^{\circ}C$ and kinematic viscosity $v = 8.71 \cdot 10^{-7}$. The water flow velocity was set to v = 0.0762m/s (3in/s) what established the Reynolds number to Re = 21526.

2.3 Particle Image Velocimetry

The experimental setup scheme for Particle Image Velocimetry (PIV) is presented in Fig. 5. Two linear lasers illuminate the tracer particles submerged in water. These lasers were positioned to ensure even illumination and minimize shadows, enhancing the accuracy of particle tracking (see Figs. 6 and 7). The experimental setup (Fig. 5) included a high-speed camera and two linear lasers, one set under the test chamber, enlightening the geometry from the downside and another set behind the test chamber, enlightening the tested geometry from behind. A high-speed camera is placed to capture the illuminated particles at high frame rates, ensuring precise temporal resolution. The captured images were processed by a dedicated software PIVLab [20], which analyzes the displacement of particles between frames to calculate the velocity field. Particle Image Velocimetry (PIV) was employed to analyze the flow characteristics around an airfoil within a water tunnel. This setup allows for detailed visualization of the flow patterns around the airfoil and measurement of the velocity distribution in the chosen plane of analysis.

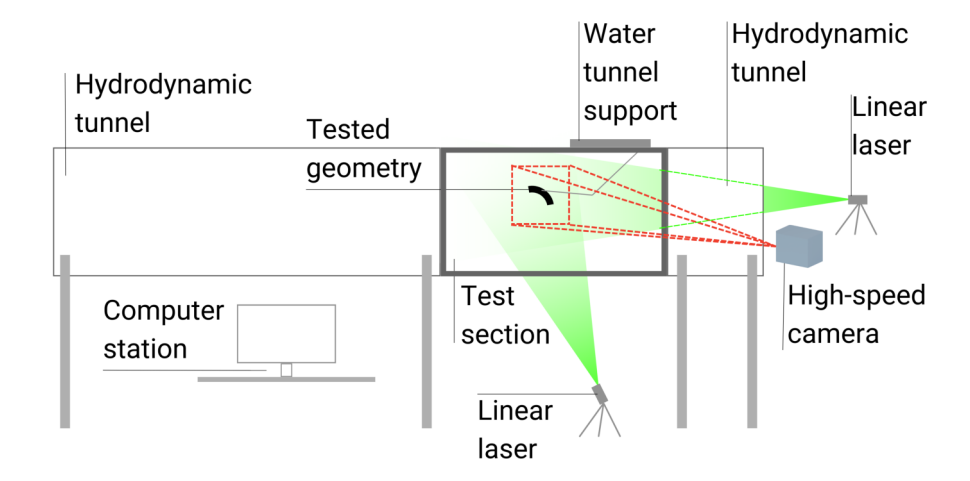


Figure 5 – Graphic representation of the experimental setup.

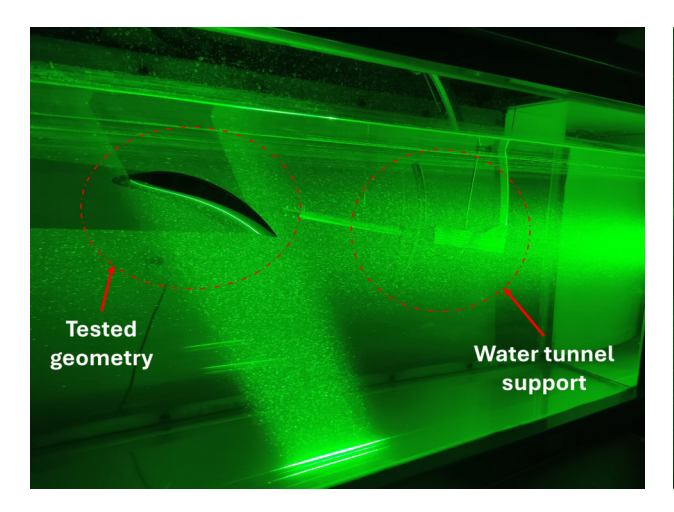


Figure 6 – Presentation of measuring chamber with tested geometry.

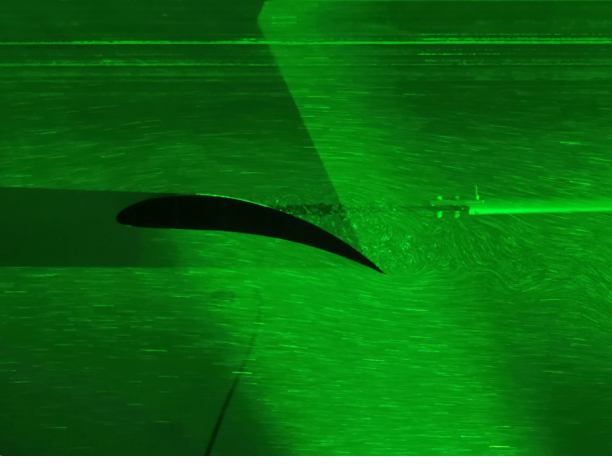


Figure 7 – Turbulence behind *Airfoil 3* geometry. View of particles enlightened by linear lasers.

2.4 Computational Fluid Dynamics

Various science papers [21, 22, 23] show the possibilities for using numerical methods to possess overall information regarding the aerodynamic characteristics of aircraft or its parts. Worth of mentioning is also, that such a method can be used in further design, starting from the influence of deflected control surfaces, influence of the propeller, and even the cooling systems of the engine and cabin could be tested [24, 25]. Also the armament drop safety can be tested [26] in order to avoid contact with the fuselage or other part of the aircraft. The numerical simulations were conducted by solving the steady-state, incompressible Navier-Stokes equations, formulated as:

$$(\mathbf{u} \cdot \nabla) \mathbf{u} = -\frac{1}{\rho} \nabla p + \nu \nabla^2 \mathbf{u}$$
 (1)

and the continuity equation, expressed as:

$$\nabla \cdot \mathbf{u} = 0 \tag{2}$$

where $\mathbf{u} = (u_x, u_y)$ denotes the fluid velocity vector, ρ is the fluid density, p represents pressure, and v denotes the kinematic viscosity. The gravity term was excluded from Equation (1) to prevent streaming flow interference. Equations (1) and (2) were discretized using the Finite Volume Method (FVM). The simulations utilized OpenFOAM, an open-source C++ toolbox. The computations employed the Semi-Implicit Method for Pressure Linked Equations (SIMPLE) solver algorithm. The turbulence model adopted was the k- ω Shear Stress Transport (SST). The convective form of equations for the steady-state k- ω SST model is expressed as [27]:

$$\nabla \cdot (\mathbf{u}k) = \frac{P}{\rho} - \beta^* \omega k + \nabla \cdot [(\nu + \sigma_k \nu_t) \nabla k]$$
(3)

$$\nabla \cdot (\mathbf{u}\omega) = \frac{\gamma}{\mu_t} P - \beta \omega^2 + \nabla \cdot [(\nu + \sigma_\omega \nu_t) \nabla \omega] + 2(1 - F_1) \frac{\sigma_{\omega 2}}{\omega} \nabla k \nabla \omega$$
 (4)

where ρ is the fluid density, k is the turbulent kinetic energy, ω is the specific dissipation rate, \mathbf{u} is the fluid velocity vector, μ_t is the turbulent eddy viscosity, v is the kinematic viscosity, v_t is the turbulent kinematic viscosity, σ_k is the turbulent Prandtl number for k, σ_{ω} is the turbulent Prandtl number for ω , P is the production term, F_1 is the blending function. Variables such as β , β^* , γ , σ_k , σ_{ω} , $\sigma_{\omega 2}$ are constants.

2.4.1 Computational domain

The standard guidelines for 2D subsonic aerodynamic simulations suggest a minimum domain length of 5c or ideally $\geq 100c$ [28, 29, 30]. However, these guidelines are generalized for external aerodynamics and should be adjusted based on real-world Reynolds numbers and flow conditions. Feasibility and computing power are also crucial factors to consider. When determining the computational domain size, the main concern is the error caused by placing the domain boundaries too close to the studied object [31]. In this preliminary study of morphing airfoils, where flow conditions involved low Reynolds numbers, very low flow velocity, and water as the medium, we opted for smaller domain dimensions of 30c. This decision strikes a balance between potential errors, as discussed on the NASA website [31] and in other studies [32]. Many airfoil studies suggest similar domain dimensions, as evidenced by [33, 34]. For meshing the airfoils, we utilized the snappyHexMesh utility provided by the OpenFOAM package. This tool generates hex-dominant meshes from triangulated geometries and adds layers during the meshing process. Given that the focus of our study was Particle Image Velocimetry (PIV) experiments, we prioritized cell refinement near the airfoil to achieve high-resolution results for comparison with PIV images. The numerical mesh development involved two parts: the computational domain and the circular shape containing the airfoil. The computational domain mesh included an opening where the numerical mesh of the airfoil was inserted and stitched together. This approach allows for easy rotation of the airfoil in future simulations. These methods are commonly employed by researchers, as demonstrated by [34, 35]. Figure 8 depicts a conceptual representation of the computational domain, highlighting distances and dimensions.

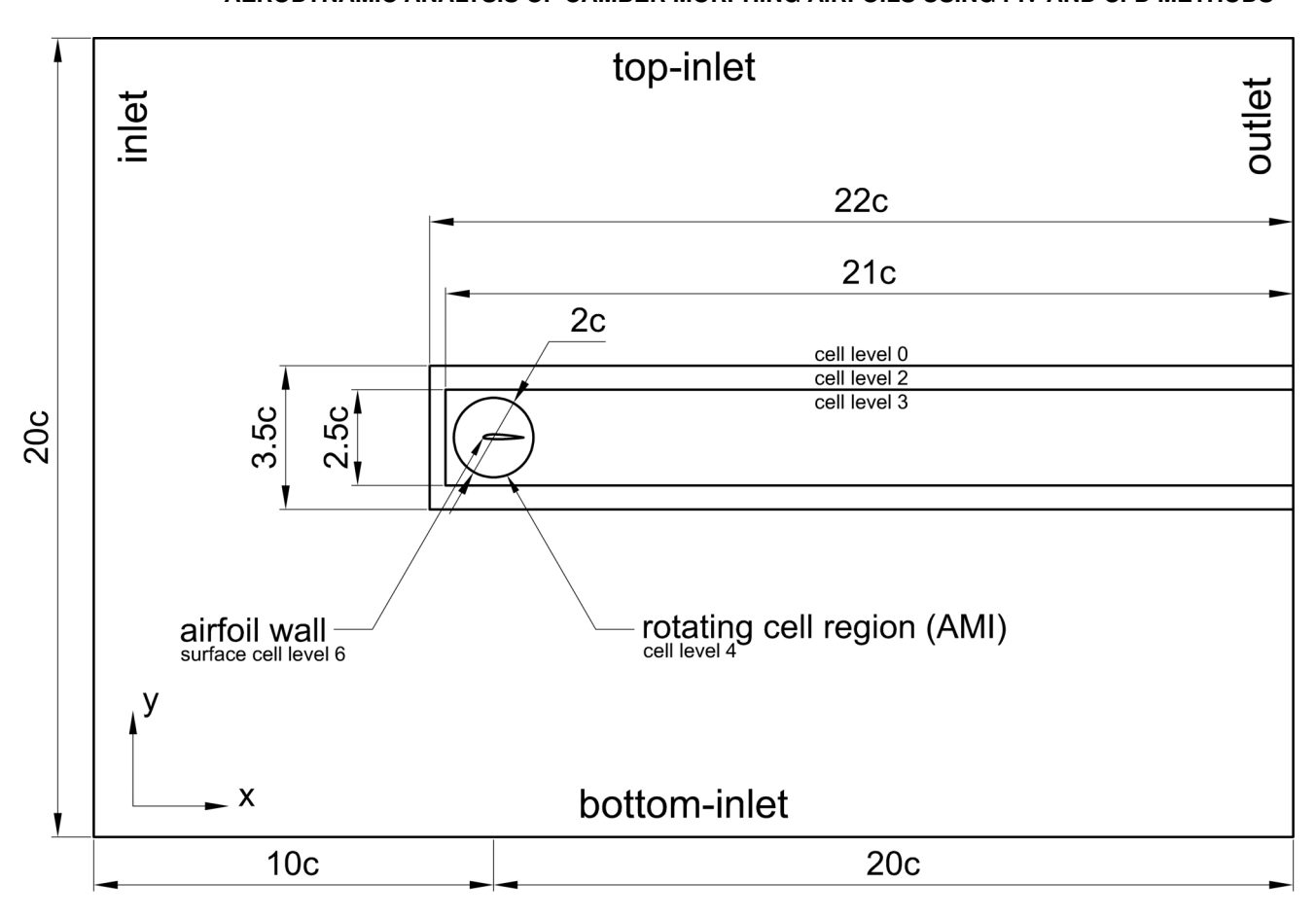


Figure 8 – Computational domain and boundary conditions for the airfoil simulation

The airfoil chord length, denoted as c, dictated the domain size. The domain extended 10c in the front, top, and bottom of the airfoil, and 20c behind it, resulting in dimensions of 30c along the x-axis and 20c along the y-axis. A smaller dimension was chosen for the y-axis to accommodate the consistent inflow direction across cases. Manipulating the angle of attack involved rotating the inner cell-zone containing the airfoil, maintaining the primary flow direction along the x-axis until reaching the airfoil. The y-axis dimensions were tailored to address flow deflection and turbulent effects induced by the airfoil. Employing 20c dimensions downstream of the airfoil adequately captured the resulting flow pattern. As the cases were two-dimensional (2D), the z-axis dimension was irrelevant. The mesh center point, (x,y) = (0,0), served as the airfoil aerodynamic center. The rotating cell zone had a diameter of 2c to accommodate the airfoil and refine cells properly around it. The numerical grid underwent refinement near the airfoils and in their slipstream, totalling approximately 3,370,000 cells. To model the viscous sublayer, n = 25 layers with an inflation factor of $\delta = 1.2$ were generated, ensuring y+<1 for all geometries. Key features of the numerical grids are depicted in Figure 9.

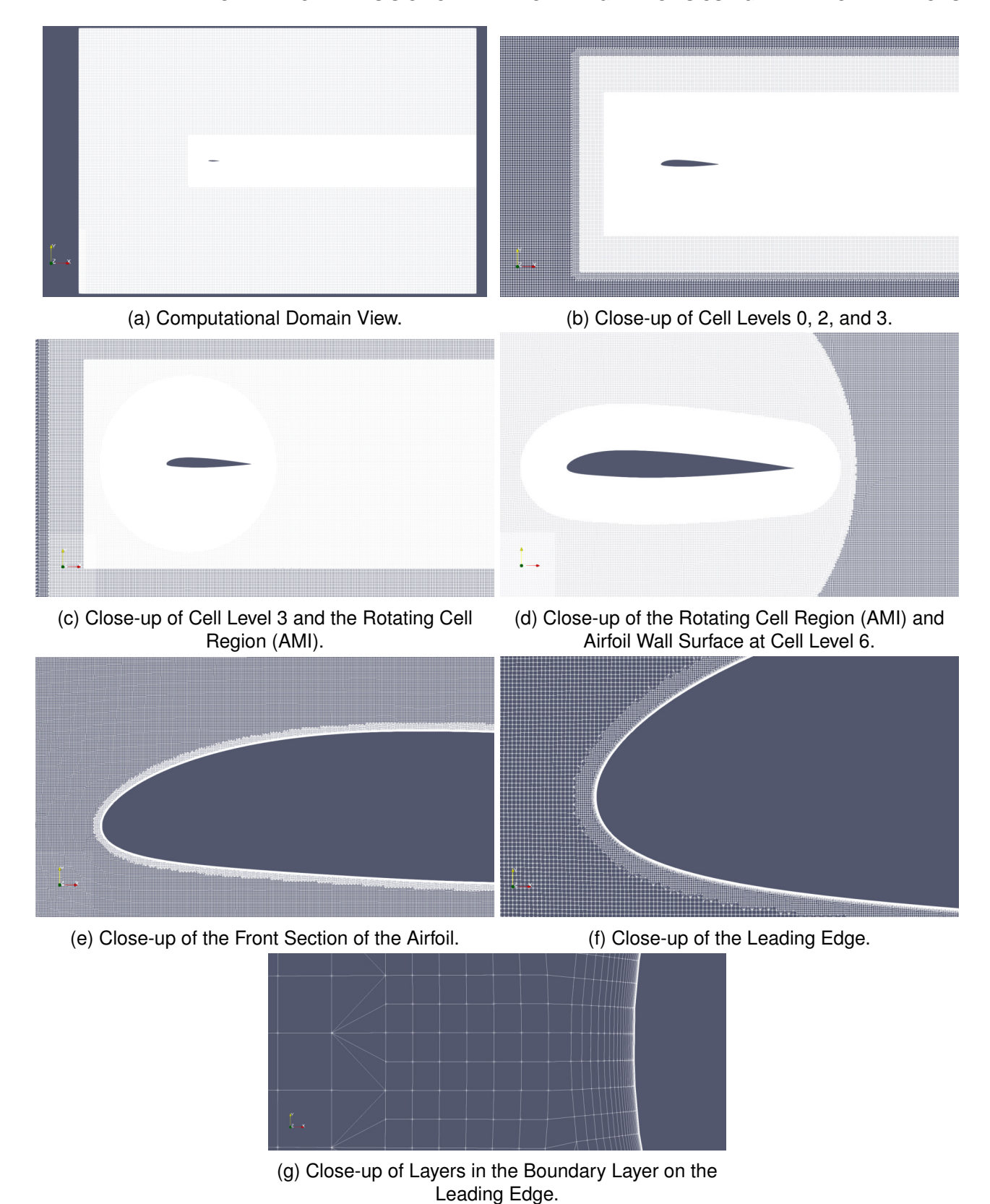


Figure 9 – An in-depth examination of critical sections of the numerical grid reveals the following for *Airfoil 1*.

2.4.2 Discretization schemes

The performed calculations were 2nd order accurate, due to majority of schemes being 2nd order, with a small exception of $\nabla \cdot (\phi k)$ and $\nabla \cdot (\phi \omega)$, which were 1st order schemes, in order to provide better stability of the simulations. This was recommended due to their diffusive nature by OpenFOAM user guide [36, 37, 38].

2.4.3 Flow characteristics and boundary conditions

Numerical simulations were conducted to analyze 2D hydrodynamics around airfoil geometries under steady-state conditions. The flow, characterized as subsonic with very low Mach numbers and Reynolds numbers (Re = 19,400 - 21,900), adhered to the material properties of water at 26.3°C. The material was a single-phase, non-reacting, and incompressible Newtonian fluid, with an inflow velocity maintained at a constant U = 0.0762 m/s. To calculate the initial values of k and ω , Equations (6) -(8) [39] were employed. The velocity components u_x and u_y were derived from the velocity magnitude **u** and the angle of attack α . The equations for k, ω , and ω_{wall} were sourced from the OpenFOAM user guide [39] and are presented below:

$$(u_x, u_y) = (\mathbf{u}\cos\alpha, \mathbf{u}\sin\alpha) \tag{5}$$

$$k = \frac{3}{2}(\mathbf{u}I)^2 \tag{6}$$

$$k = \frac{3}{2} (\mathbf{u}I)^2$$

$$\omega = \frac{k^{0.5}}{C_{\mu}^{0.25} \cdot L}$$
(6)
(7)

$$\omega_{wall} = \frac{6v}{\beta_1 v^2} \tag{8}$$

where I is the turbulence intensity, \mathbf{u} is the velocity magnitude inside the domain, C_{μ} is a constant of 0.09, L is the reference length scale, v is the kinematic viscosity, β_1 is a constant of 0.075, and y is the wall normal distance. The convergence criterion for steady-state simulations relied on residual control for velocities $(u_x|u_y \le 1 \times 10^{-6})$, kinematic pressure $(p \le 1 \times 10^{-6})$, turbulent kinetic energy and specific dissipation rate ($k|omega \le 1 \times 10^{-6}$). Once all residuals reached the specified threshold, the simulations automatically halted. In cases where these criteria were not met, a backup convergence criterion was implemented, requiring a total number of iterations n = 35000.

3. Results and Discussion

In this research, the authors present results for one representative example of morphing-camber airfoil geometry with reference to the setting angle of the airfoil. The preliminary research comparing six prepared geometries and enlightening differences resulting from trailing edge deflections are presented in [1]. The validation of the numerical simulations model was based on velocity field distribution graphic representation. Though the experimental and numerical results are not identical, they are comparable and allow us to validate the numerical model. Three examples of velocity field distribution for different setting angles are presented in Figure 10.

Due to the mentioned in section 2.2ow Reynolds number and low velocity of the stream, the wake structure was continuously forming and separating from the airfoil (Fig. 10 CFD results). The turbulence resulting from this phenomenon is visible in Figure 10 PIV results, as the experimental PIV velocity distribution is obtained from 500 successive frames averaged to one graphic representation. Both methods present similar velocity distributions, but CFD simulations have a tendency to overestimate velocity over the wake structure. The size of the wake structure is increasing with the increase of the setting angle. The velocity over airfoil's wake structure is also increasing with the increase of the setting angle. The greater the wake structure and stream disturbance, the higher the values of the drag coefficient. This observation is consistent with obtained drag force coefficient characteristics (Fig. 11, which shows a nearly constant increase of drag with the increase of setting angle. The exception is -10° setting angle, where the drag coefficient is higher than for -8° setting angle.

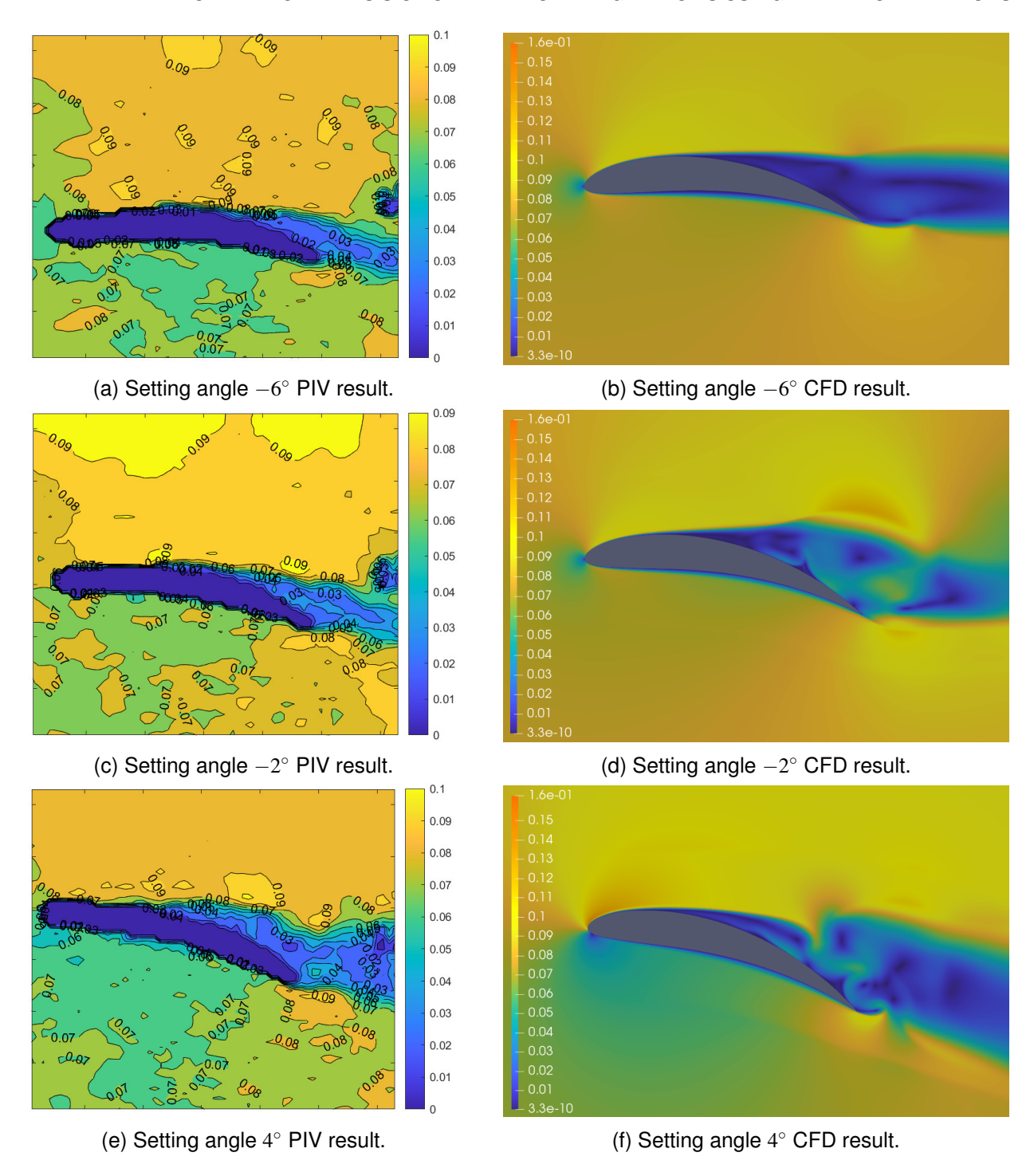


Figure 10 – Airfoil 3 PIV and CFD velocity distribution for three example setting angles.

Lift force coefficient characteristics are non-conventional. For the -10° to -6° setting angles, the lift force coefficient characteristics are descending. From setting angle -6° to 0° , the characteristic rises linearly, then flattens, and the highest lift force coefficient value is obtained for the 6° setting angle. Pitching moment coefficient characteristics show a rising tendency, which suggests static instability of proposed geometry with the increase of setting angle. The specific values of the pitching moment coefficient are dispersed. It is the result of the centre of pressure's changing position, with the wake structure fluctuations and periodic separation.

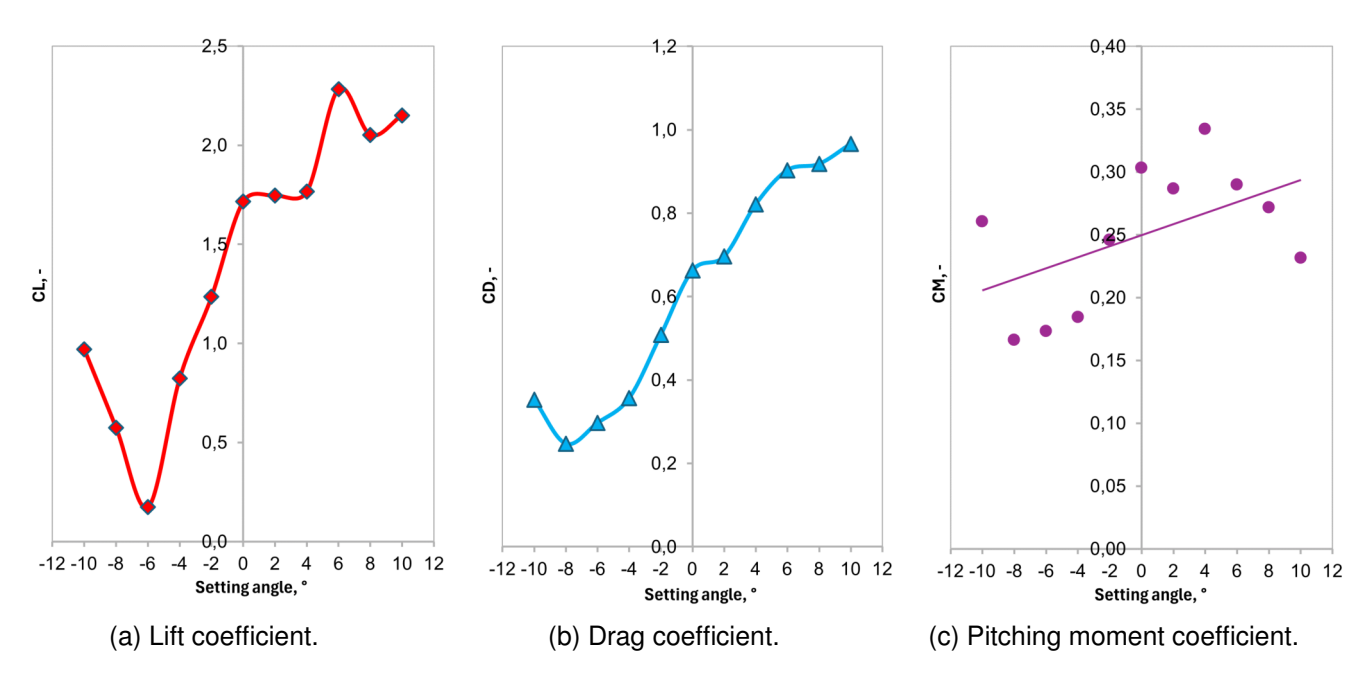


Figure 11 – Airfoil 3 coefficients characteristics for examined setting angles.

4. Conclusions

In this paper, the authors present experimental and numerical research methods and obtain results for a representative example of a cambered morphing airfoil. The experiments were conducted in a hydrodynamic tunnel using Particle Image Velocimetry for velocity field representation. The numerical model was validated based on velocity distribution. Numerical simulations obtained the coefficient characteristics. The lift force coefficient characteristics have a non-conventional shape, but the lift force coefficient mostly increases with the increase of the setting angle. The drag force coefficient increases with the setting angle. The exception is the -10° setting angle, where the drag is slightly higher than for the -8° setting angle. The pitching moment coefficient suggests the presented morphing camber airfoil to preserve static instability. The results are very promising and are in line with expectations. This solution is an innovative approach to morphing airfoils as most of the research focuses on decreasing drag, while the authors of this work created the geometry that can create drag. In the next phase of research, the authors would like to perform a detailed examination of proposed geometries on micro UAV aircraft. With the rough development of shape-morphing materials. miniaturisation, and technological solutions for morphing airfoils, this could be a promising solution for micro UAVs to decrease the risk of damage in the landing phase and improve aerodynamic efficiency in wind gusts.

5. Contact Author Email Address

Mailto: lukasz.kiszkowiak@wat.edu.pl

6. Funding

The paper was elaborated basing on data obtained during the research carried out in the following project:

A multi-sensor platform for imaging and detecting threats occurring in areas with high dynamics of changes in environmental conditions - DOB-SZAFIR/01/B/038/04/2021 – funded by the National Centre for Research and Development;

that was implemented in the Military University of Technology.

7. Copyright Statement

The authors confirm that they, and/or their company or organization, hold copyright on all of the original material included in this paper. The authors also confirm that they have obtained permission from the copyright holder of any third-party material included in this paper to publish it as part of their paper. The authors confirm that they give permission, or have obtained permission from the copyright holder of this paper, for the publication and distribution of this paper as part of the ICAS proceedings or as individual off-prints from the proceedings.

References

- [1] Marta Marciniuk, Paweł Piskur, Łukasz Kiszkowiak, Łukasz Malicki, Krzysztof Sibilski, Katarzyna Strzelecka, Stanisław Kachel, and Zygmunt Kitowski. Aerodynamic analysis of variable camber-morphing airfoils with substantial camber deflections. Energies, 17(8):1801, 2024.
- [2] Terrence A Weisshaar. Morphing aircraft systems: historical perspectives and future challenges. <u>Journal</u> of aircraft, 50(2):337–353, 2013.
- [3] Bruce W Jo and Tuba Majid. Aerodynamic analysis of camber morphing airfoils in transition via computational fluid dynamics. Biomimetics, 7(2):52, 2022.
- [4] Tuba Majid and Bruce W Jo. Comparative aerodynamic performance analysis of camber morphing and conventional airfoils. Applied Sciences, 11(22):10663, 2021.
- [5] Faiyaz Ahmed, JC Mohanta, Anupam Keshari, and Pankaj Singh Yadav. Recent advances in unmanned aerial vehicles: a review. Arabian Journal for Science and Engineering, 47(7):7963–7984, 2022.
- [6] Aleksander Olejnik, Łukasz Kiszkowiak, Robert Rogolski, Grzegorz Chmaj, Michał Radomski, Maciej Majcher, and Łukasz Omen. The use of unmanned aerial vehicles in remote sensing systems. Sensors, 20(7):2003, 2020.
- [7] Syed Agha Hassnain Mohsan, Nawaf Qasem Hamood Othman, Yanlong Li, Mohammed H Alsharif, and Muhammad Asghar Khan. Unmanned aerial vehicles (uavs): Practical aspects, applications, open challenges, security issues, and future trends. Intelligent Service Robotics, 16(1):109–137, 2023.
- [8] H Ryaciotaki-Boussalis and D Guillaume. Computational and experimental design of a fixed-wing uav. Handbook of Unmanned Aerial Vehicles, Springer, pages 109–141, 2015.
- [9] Shiva Sharma, Umran Sharieff, Ankit Singh, and RS Tarnacha. Design and fabrication of fixed-wing uav for commercial monitoring. Int. J. Eng. Res. Technol, 8:1153–1177, 2021.
- [10] Leszek Cwojdziński. <u>Bezzałogowe Systemy Walki-charakterystyka, wybrane problemy użycia i</u> eksploatacji. Wojskowa Akademia Techniczna, 2014.
- [11] Maciej Miszczak, Piotr Ruliński, Bohdan Zarzycki, and M Kuc. An application of visual-observation unmanned aerial vehicles in live firing range tests. Problemy Mechatroniki: uzbrojenie, lotnictwo, inżynieria bezpieczeństwa, 9, 2018.
- [12] Andres E Rivero, Stephane Fournier, Marinos Manolesos, Jonathan E Cooper, and Benjamin KS Woods. Experimental aerodynamic comparison of active camber morphing and trailing-edge flaps. AIAA Journal, 59(7):2627–2640, 2021.
- [13] Expert pointers for better fixed-wing uav designs. https://www.micropilot.com/pdf/fixed-wing-uav-designs.pdf. Accessed: 2024-04-28.
- [14] Guillaume Jouvet, Yvo Weidmann, Eef Van Dongen, Martin P Lüthi, Andreas Vieli, and Jonathan C Ryan. High-endurance uav for monitoring calving glaciers: Application to the inglefield bredning and eqip sermia, greenland. Frontiers in Earth Science, 7:206, 2019.
- [15] Anna Michalska, Daniel Michalski, and Stepan Savchuk. Reliability of unmanned aerial vehicles: winglets' issue. Aviation and Security Issues, 2023.
- [16] Daniel Lichoń, Anna Mikołajczyk, Łukasz Kiszkowiak, and Tomasz Łącki. Identification of uav static aerodynamic characteristics in the water tunnel balance research. <u>Advances in Mechanical and Materials</u> Engineering, 33(293 (2)):127–140, 2016.
- [17] Krzysztof Sibilski, Mirosław Nowakowski, Dariusz Rykaczewski, Paweł Szczepaniak, Andrzej Żyluk, Anna Sibilska-Mroziewicz, Michał Garbowski, and Wiesław Wróblewski. Identification of fixed-wing micro aerial vehicle aerodynamic derivatives from dynamic water tunnel tests. <u>Aerospace</u>, 7(8):116, 2020.
- [18] RHRC Animus. Research water tunnel specification. El Segundo California, User's Manual, 2009.
- [19] M Kerho and B Kramer. Five-component balance and computer-controlled model support system for water tunnel applications. Rolling Hills Research Corporation (RHRC): El Segundo, CA, USA, 2009.
- [20] William Thielicke and René Sonntag. Particle image velocimetry for matlab: Accuracy and enhanced algorithms in pivlab. <u>Journal of Open Research Software</u>, 9(1), 2021.

- [21] Tomasz Goetzendorf-Grabowski and Agnieszka Kwiek. Study of the impact of aerodynamic model fidelity on the flight characteristics of unconventional aircraft. Applied Sciences, 13(22), 2023.
- [22] Agnieszka Kwiek, Marcin Figat, and Tomasz Goetzendorf-Grabowski. The study of selected aspects of the suborbital vehicle return flight trajectory. Aerospace, 10(5), 2023.
- [23] Aleksander Olejnik, Łukasz Kiszkowiak, Piotr Zalewski, and Adam Dziubiński. Low-cost satellite launch system—aerodynamic feasibility study. <u>Aerospace</u>, 9(6), 2022.
- [24] Zdobyslaw Goraj, Andrzej Frydrychewicz, Stanislaw Danilecki, Aleksander Olejnik, and Łukasz Kiszkowiak. Conceptual design of a third generation aerobatic aircraft. Proceedings of the Institution of Mechanical Engineers, Part G: Journal of Aerospace Engineering, 237:095441002211363, 11 2022.
- [25] Gustavo Luiz Olichevis Halila, Alexandre Pequeno Antunes, Ricardo Galdino da Silva, and João Luiz F. Azevedo. Effects of boundary layer transition on the aerodynamic analysis of high-lift systems. <u>Aerospace</u> Science and Technology, 90:233–245, 2019.
- [26] Aleksander Olejnik, Adam Dziubiński, and Łukasz Kiszkowiak. Separation safety analysis using cfd simulation and remeshing. Aerospace Science and Technology, 106:106190, 2020.
- [27] The menter shear stress transport turbulence model. https://turbmodels.larc.nasa.gov/sst. html. Accessed: 2024-05-06.
- [28] Bengt Fornberg. A numerical study of steady viscous flow past a circular cylinder. <u>Journal of Fluid</u> Mechanics, 98(4):819–855, 1980.
- [29] James L Thomas and MD Salas. Far-field boundary conditions for transonic lifting solutions to theeuler equations. AIAA journal, 24(7):1074–1080, 1986.
- [30] Falk Goetten, D Felix Finger, Matthew Marino, Cornelis Bil, Marc Havermann, and Carsten Braun. A review of guidelines and best practices for subsonic aerodynamic simulations using rans cfd. In <u>APISAT</u> 2019 Asia Pacific International Symposium on Aerospace Technology, pages 227–245, 2019.
- [31] Effect of farfield boundary. https://turbmodels.larc.nasa.gov/naca0012_val_ffeffect.html. Accessed: 2024-05-06.
- [32] Narges Golmirzaee and David H Wood. Some effects of domain size and boundary conditions on the accuracy of airfoil simulations. Advances in Aerodynamics, 6(1):1–27, 2024.
- [33] SM Rakibul Hassan, Toukir Islam, Mohammad Ali, and Md Quamrul Islam. Numerical study on aerodynamic drag reduction of racing cars. Procedia Engineering, 90:308–313, 2014.
- [34] F Geng, I Kalkman, ASJ Suiker, and B Blocken. Sensitivity analysis of airfoil aerodynamics during pitching motion at a reynolds number of 1.35× 105. <u>Journal of Wind Engineering and Industrial Aerodynamics</u>, 183:315–332, 2018.
- [35] Łukasz Malicki, Ziemowit Malecha, and Krzysztof Tomczuk. Leading-edge vortex controller (levcon) influence on the aerodynamic characteristics of a modern fighter jet. Energies, 16(22):7590, 2023.
- [36] Openfoam v8 user guide 4.5 numerical schemes. https://doc.cfd.direct/openfoam/user-guide-v8/fvschemes. Accessed: 2024-05-06.
- [37] Openfoam numerical schemes. https://www.openfoam.com/documentation/user-guide/6-solving/6.2-numerical-schemes. Accessed: 2024-05-06.
- [38] Openfoam: User guide v2112 schemes. https://www.openfoam.com/documentation/guides/v2112/doc/guide-schemes. Accessed: 2024-05-06.
- [39] K-omega shear stress transport (sst). https://www.openfoam.com/documentation/guides/v2112/doc/guide-turbulence-ras-k-omega-sst.html. Accessed: 2024-05-06.